



Integration of MEMS IR detectors with MIR waveguides for sensing applications

MAHMUT SAMI YAZICI,^{1,2,3}  BOWEI DONG,^{1,2,4}  DIHAN HASAN,⁵
FUJUN SUN,¹ AND CHENGKUO LEE^{1,2,4,*} 

¹Department of Electrical and Computer Engineering, National University of Singapore, 117583, Singapore

²Center for Intelligent Sensors and MEMS, National University of Singapore, E6 #05-11F, 5 Engineering Drive 1, 117608, Singapore

³Centre for Advanced 2D Materials and Graphene Research Centre, National University of Singapore, 117546, Singapore

⁴NUS Graduate School for Integrative Sciences and Engineering, National University of Singapore, 117456, Singapore

⁵Department of ECE, Northsouth University, Plot, 15, Block B Kuril - NSU Rd, Dhaka 1229, Bangladesh
[*elelc@nus.edu.sg](mailto:elelc@nus.edu.sg)

Abstract: Waveguides have been utilized for label-free and miniaturized mid-infrared gas sensors that operate on the evanescent field absorption principle. For integrated systems, photodetectors based on the photocarrier generation principle are previously integrated with waveguides. However, due to the thermal excitation of carriers at room temperature, they suffer from large dark currents and noise in the long-wavelength region. In this paper, we introduce the integration of a MEMS-based broadband infrared thermopile sensor with mid-infrared waveguides via flip-chip bonding technology and demonstrate a proof-of-concept gas (N₂O) sensor working at 3.9 μm. A photonic device with input and output grating couplers designed at 3.72 μm was fabricated on a silicon-on-insulator (SOI) platform and integrated with a bare thermopile chip on its output side via flip-chip bonding in order to realize an integrated photonic platform for a myriad range of sensing applications. A responsivity of 69 mV/W was measured at 3.72 μm for an 11 mm waveguide. A second device designed at 3.9 μm has a 1800 ppm resolution for N₂O sensing.

© 2020 Optical Society of America under the terms of the [OSA Open Access Publishing Agreement](#)

1. Introduction

Mid-infrared (MIR) (2–20 μm) contains molecular vibrational fingerprints of molecules such as CO, CO₂, N₂O, NO₂ and volatile organic compounds (VOCs) that are important for air quality and human health monitoring [1,2]. For real-time monitoring of the concentration of these molecules in air, electrochemical or non-dispersive infrared (NDIR) sensors are utilized [3,4]. Electrochemical sensors can be made in small footprints, but they suffer from non-linearity, slow response, and low accuracy [5–8]. NDIR sensors, on the other hand, show linear and fast response and possess high accuracy [9,10]. However, for high accuracy, longer interaction lengths are required and hence make the overall system bulkier. Recently, waveguide-based gas sensors are proposed as an alternative to NDIR sensors [11–16]. These sensors are based on target gas molecules interacting with the evanescent field and absorption of light at the target molecule's fingerprint frequency [17–19] and hence decrease in the transmission. The waveguide length which defines the interaction length with the target gas can be made significantly longer in a smaller area by utilizing multiple turns of the waveguide on a single chip [12]. Utilizing low loss materials in MIR such as recently explored chalcogenides for the operation wavelength with small propagation loss (<1 dB/cm) paves the way for high Q resonators and long waveguides for highly responsive sensors and spectrometers [20–22]. For realizing IR spectrometers, infrared sources [23–25] and photodetectors are integrated with waveguides either by monolithic fabrication of

waveguide and detector [26,27] or by transferring of a low dimensional material based detector onto the grating coupler area [28,29]. However, the detectors used so far are based on the photocarrier generation principle. Hence, their performance is limited in the long-wave infrared (LWIR) range where the thermal excitation of carriers generates large dark currents and noise, decreasing the signal to noise ratio (SNR) limiting the overall performance [30]. To mitigate large dark currents, active cooling of the detectors to cryogenic temperatures is required, which limits the application of these detectors. On the other hand, MEMS-based IR detectors such as thermopiles and microbolometers are commonly used in the LWIR range and even extending to the far-infrared (FIR) and THz range [31–33] without any need for cooling [34,35]. In this paper, we report the integration of a broadband thermopile IR detector with a MIR waveguide via thermo-compression type flip-chip bonding technology [36]. Furthermore, we demonstrated N₂O sensing with a second device designed at the absorption wavelength (3.89 μm) of the target gas. Integrating a broadband thermopile device with the photonics chip demonstrates the first step towards fully integrated chip-scale photonics gas sensors and spectrometers.

2. Device fabrication

The Si-based waveguide and grating coupler are fabricated on a silicon-on-insulator (SOI) wafer with 0.5 μm device layer and 2 μm buried oxide (BOX). The design of the grating couplers is optimized using a finite-difference time-domain (FDTD) simulation software. Waveguide and grating couplers on either side are defined via electron beam lithography (EBL) and reactive ion etching (RIE) of the device layer (Fig. 1). Ni/Au (15nm/150nm) electrodes on the photonics device are patterned via a laser writer and metals are deposited using sputtering. Following lift-off (Fig. 2(a)), aluminum (Al) wedges (Fig. 2(b)) are formed using wire-bonding tool with an Al wire diameter of 25 μm both on the photonics and thermopile chips. Al serves as the metal interconnect between the thermopile and photonics chip to allow electrical connection

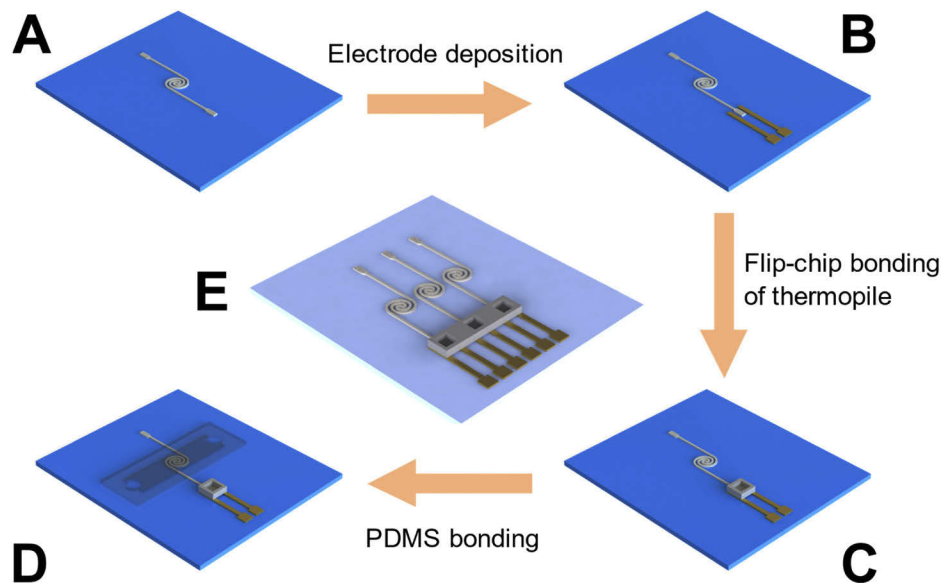


Fig. 1. Schematic for the process flow starting with an SOI wafer. A) Device outlook after waveguide patterning. B) Device outlook after metal electrode deposition. C) Device outlook after flip-chip bonding of thermopile device onto photonics chip. D) Device outlook after PDMS gas chamber bonding onto photonics chip. E) Proposed device schematic for arrayed waveguide/thermopile pairs for multi-gas sensing and spectrometer applications.

to thermopile. Meanwhile, it also forms the spacer layer with a gap of $10\ \mu\text{m}$ (Fig. 2(c) and Fig. 3) between the two chips. Finally, the thermopile chip is flipped and bonded on top of the photonic chip via thermo-compression bonding. The thermopile active area is carefully aligned with the output grating coupler to maximize the responsivity. The bonding is performed at a 300°C stage temperature and 400°C arm temperature (arm holding the flipped chip) and constant force of $5\ \text{N}$ is applied for 5 minutes during the bonding process. For the gas sensing experiment, a PDMS microchamber was formed from a 3D-printed veroclear mold and was bonded onto the spiral waveguide (Fig. 2(d) after oxygen (O_2) plasma treatment of both PDMS and Si-waveguide surfaces.

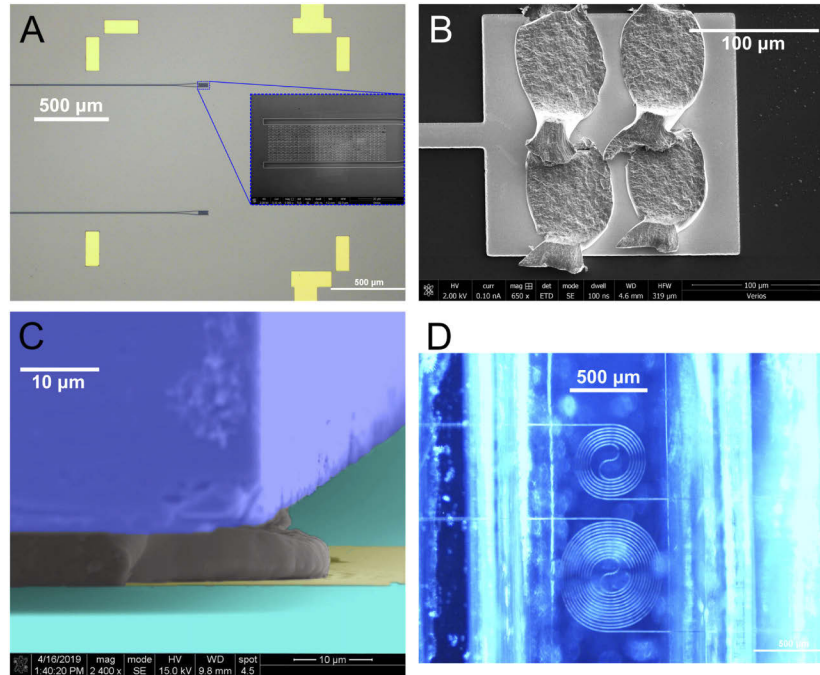


Fig. 2. A) Optical image of grating coupler area (with an inset SEM image) after waveguide fabrication and metal deposition. B) SEM image of Al-wedges formed on Au-pads. C) False-color SEM image of thermopile-waveguide interface. (TP in purple, photonics chip in green, Au-pad in yellow and Al-interface in grey) D) Darkfield optical image of spiral waveguides integrated with the PDMS chamber.

The bonding result is shown in Fig. 2(c) with a false-color SEM image (thermopile chip in purple, photonics chip in green, gold pads in yellow and Al interface in grey). After bonding, we have measured the gap between the photonics layer and the thermopile layer by using SEM. The gap of $\sim 4\ \mu\text{m}$ and $\sim 10\ \mu\text{m}$ are measured when Al wedges are formed on one side and on either side of the interface respectively. The spacer gap can be adjusted by varying the number of Al-wedge layers and by applying different pressures and temperatures during the bonding. The bonding interface was strong enough to survive multiple drop tests from heights $> 5\ \text{cm}$.

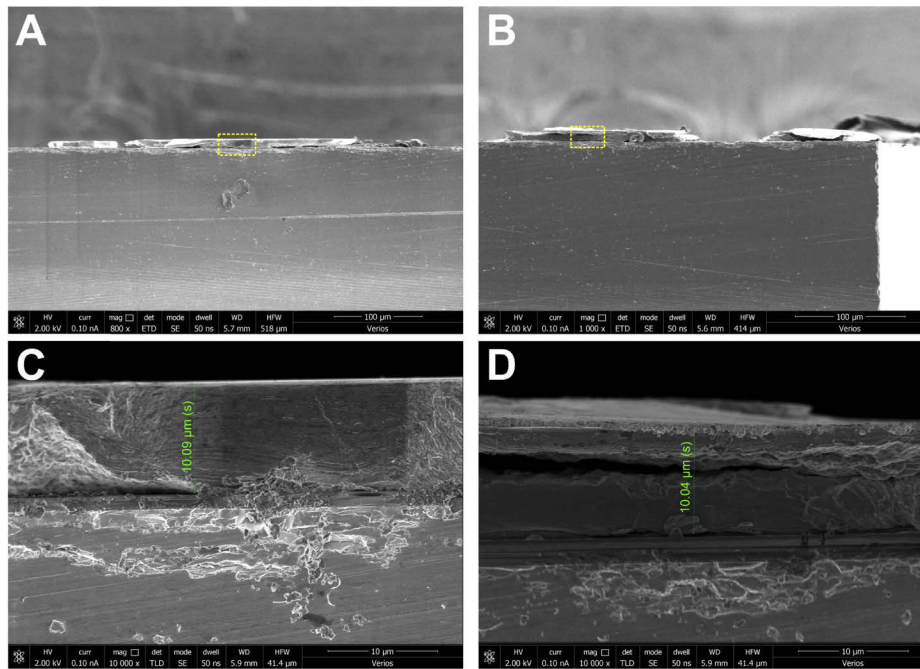


Fig. 3. SEM micrographs of the Al interface after bonding and splitting of thermopile and photonics chips. a) SEM micrograph of a bonding interface on one of the 8 pads on thermopile (left corner of the device). b) SEM micrograph of a bonding interface on one of the 8 pads on thermopile (right corner of the device). c) Zoomed SEM micrograph of the area denoted with a yellow marker in (a). d) Zoomed SEM micrograph of the area denoted with a yellow marker in (b).

3. Device characterization

The optical characterization setup (shown in Fig. 4) consists of a MIR laser system (Daylight Solution, MIRcat1200) with two continuous-wave (CW) tunable quantum cascade laser (QCL) modules (3.60-3.81 μm & 3.81-4.12 μm tuning range), an optical chopper (Stanford Research SR540), a half-wave plate for polarization control (Thorlabs, WPLQ05M-4000) and a condenser lens (ZnSe) for coupling the free-space MIR light into a MIR fiber (Thorlabs, P1-23Z). The MIR light is then coupled into the waveguide via a grating coupler. The alignments were performed by using movable stages. Prior to the integration of thermopile, the spectrum of the fabricated photonic device is measured with a commercial photodetector (Thorlabs, PDA20H) via an output fiber (not shown in Fig. 4) at a chopping frequency of 227 Hz. After the thermopile integration, the output signal is generated by the thermopile and is delivered to the lock-in amplifier (Stanford Research, SR830).

The laser power measured at the output of the laser system is ~ 300 mW at 3.75 μm (Fig. 5(a)). The power output from the fiber onto the sample is measured to be 65 mW at 3.75 μm . Spectral measurements were performed with 5 nm wavelength steps.

For gas sensing experiments, carbon dioxide (CO_2) gas was used as the reference gas and nitrous oxide (N_2O) was used as the target gas. They were fed into the PDMS gas chamber on waveguides via gas tubes.

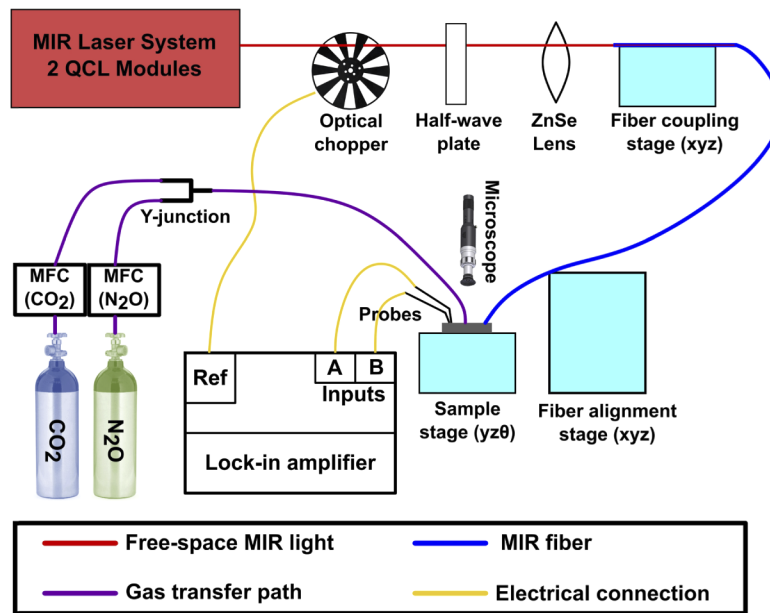


Fig. 4. Conceptual block diagram of waveguide measurement setup.

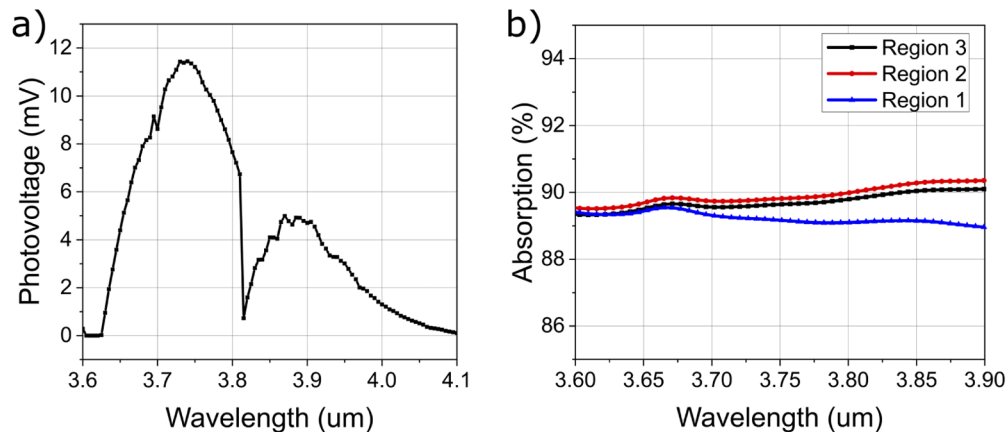


Fig. 5. a) Measured laser spectrum which is used to determine the intrinsic grating coupler/waveguide spectrum. b) Absorption spectrum of thermopile active area.

4. Analysis and discussion

The integrated device was characterized using a continuous illumination (i.e without chopper) and its responsivity was measured to be 69 mV/W [37]. In order to investigate the influence of thermopile integration on the waveguide spectrum, we compared the spectrum before and after the thermopile integration. First, the photonic device spectrum was measured with a commercial photodetector (PD) and a lock-in amplifier with an optical chopper working at 227 Hz before the thermopile integration (Fig. 6, grey line). Next, the spectrum was remeasured using the thermopile's (TP) output after the integration with different chopping frequencies (Fig. 6, colored lines). The spectral difference between the two measurements is mainly due to the fact that before integration of the thermopile, out-putted light is collected by a fiber, hence two grating couplers

contribute to the spectrum whereas before the integration, only the input grating coupler has a significant effect on the spectrum. The grating coupler efficiency at the output is constant (at $\sim 50\%$) regardless of the wavelength, when the light is coupled into the free space and not into the fiber where a mode-matching constraint is no longer present [24]. The absorption spectrum of the thermopile is measured using Fourier-transform IR spectroscopy (FTIR) in three different regions (Fig. 5(b)) of the thermopile whereas Region 1 is the middle portion of thermopile which corresponds the area right above the grating coupler and the others are slightly off from the middle part which still may receive some signal. In all cases, the spectra are relatively flat implying that the thermopile has a negligible effect on the measured photovoltage spectrum.

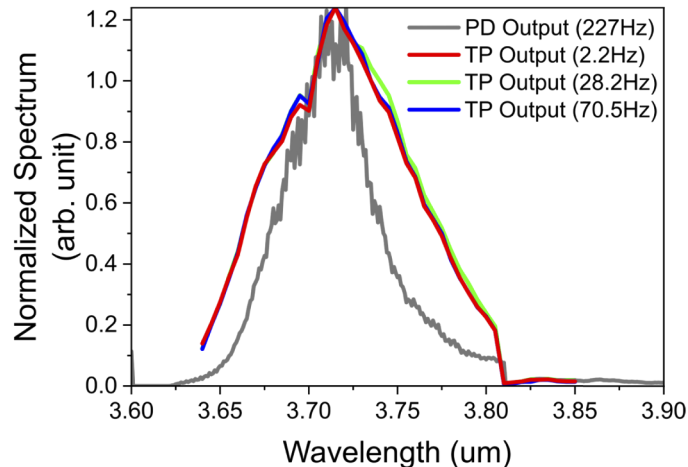


Fig. 6. Optical spectra of fabricated photonic chip (in grey) and photonics chip integrated with thermopile (in red, green and blue). Different colored graphs represent photovoltage outputs at different chopping frequencies.

After the successful integration of thermopile and photonics chip, we proceed to investigate its application as a nitrous oxide (N_2O) sensor. N_2O is a greenhouse gas and is a dominant ozone depleting compound [38,39]. It is also used in surgery for its anaesthetic and pain relieving effects [40]. Thus, it is important to measure N_2O concentrations accurately for environmental monitoring and for medical use. Hence, a specific grating coupler was designed and fabricated to operate at around $3.9\mu m$ where nitrous oxide (N_2O) has molecular absorption bands ([34], Fig. 7). Two such waveguides with spiral designs and different lengths (9.92 mm of straight waveguide and 7.51/18.41 mm of spiral waveguide for short/long spiral waveguides) were fabricated using the same fabrication steps explained above. After thermopile bonding, a PDMS chamber is bonded onto the spiral area of the waveguide to form a gas chamber and to allow gas interaction with the evanescent field of the spiral waveguide. Dark field optical image is depicted in Fig. 2(d). PDMS chamber is fabricated using a 3D-printed VeroClear master mold and bonded onto photonic chip after oxygen (O_2) plasma treatment of both PDMS and photonic device surfaces.

After thermopile and PDMS bonding; we have measured the frequency spectra of the bare thermopile device (before bonding), thermopile device bonded to $3.7\mu m$ waveguide, and thermopile device bonded to $3.9\mu m$ waveguide. The resulting frequency spectra are plotted in Fig. 8(a). The curves are fitted with a low-pass filter equation given in Eq. (1) whereas the photovoltage response is a function of the DC (0 Hz) responsivity, frequency f and thermal time constant τ . Decreased time constants of 1.87 ms (for $3.72\mu m$ WG) and 4.99/4.80 ms (for short/long WGs at $3.9\mu m$) are extracted from the fits whereas the initial time constant

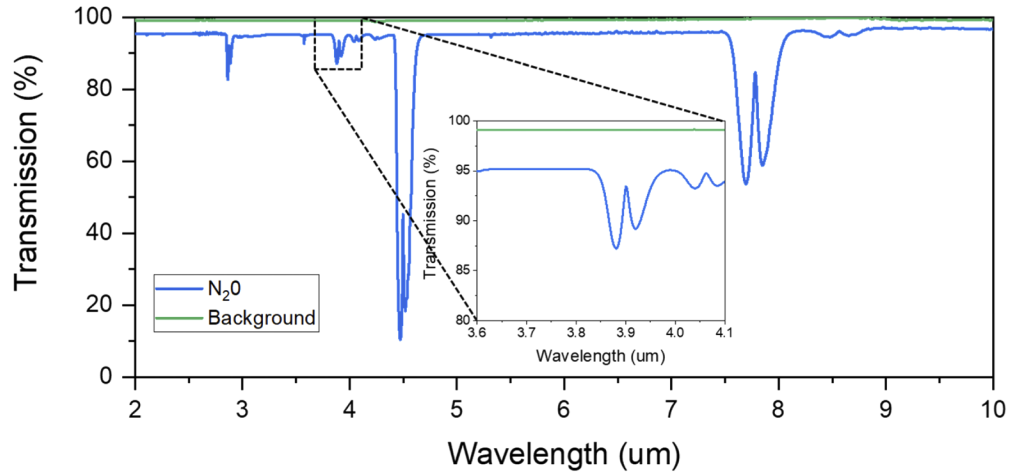


Fig. 7. Measured FTIR transmission spectrum of $N_2O_{(g)}$.

for bare (unbonded) thermopile is 28.88 ms. Reduced time constant implies that there is a thermal conduction path from the thermopile surface to the photonics chip due to a short air gap in-between the thermopile and photonic chip which increases the overall thermal conductance of the thermopile, hence resulting in a reduced time constant due to the relation provided in Eq. (2) whereas R_{th} is the thermal resistance and C_{th} is thermal capacitance. Hence, bonding of the thermopile reduces the time constant and increases the 3 dB bandwidth, however at a cost of reduced responsivity of the thermopile. Equation (3) provides the relation between the thermal resistance of thermopile and its responsivity for conventional thermopile designs whereas the thermopile consists of an absorber area in the middle and thermocouple beams surrounding the absorber area. The responsivity (R_v) of a thermopile is proportional to the number of thermocouples (N), the thermal resistance (R_{th}) and Seebeck coefficient (s) of the thermoelectric material used as the thermocouple pairs. Thus, integration caused thermal resistance reduction to decrease the thermal time constant but also decreases the responsivity of the device. Hence, for the applications requiring high responsivity, such as high accuracy gas detectors, the gap between the thermopile and waveguide chip should be increased further in order to increase the overall thermal resistance of the thermopile device.

$$V(f) = \frac{V_0}{\sqrt{1+(2\pi f\tau)^2}} \quad (1)$$

$$\tau = R_{th}C_{th} \quad (2)$$

$$R_v = NR_{th}s \quad (3)$$

Photovoltage spectra of spiral waveguides with grating couplers designed for $3.9\mu m$ are measured (using the setup depicted in Fig. 4), and the results are shown in Fig. 8(b) with solid lines showing the spectra as measured and dash-dotted lines showing the normalized spectra with respect to the laser spectrum (Fig. 5). The normalized spectra reveal the intrinsic grating coupler spectrum. Both spiral waveguides support transmission at $3.9\mu m$ wavelength so that they can be used for N_2O sensing. Both spectra of short and long spiral waveguides are measured in ambient air conditions and when the N_2O gas pumped into the PDMS gas chamber (Figs. 8(c) and 8(d)). For both waveguides, photovoltage measured from thermopile at $3.89\mu m$ wavelength (which corresponds to a stronger absorption peak of N_2O as opposed to $3.91\mu m$ absorption peak

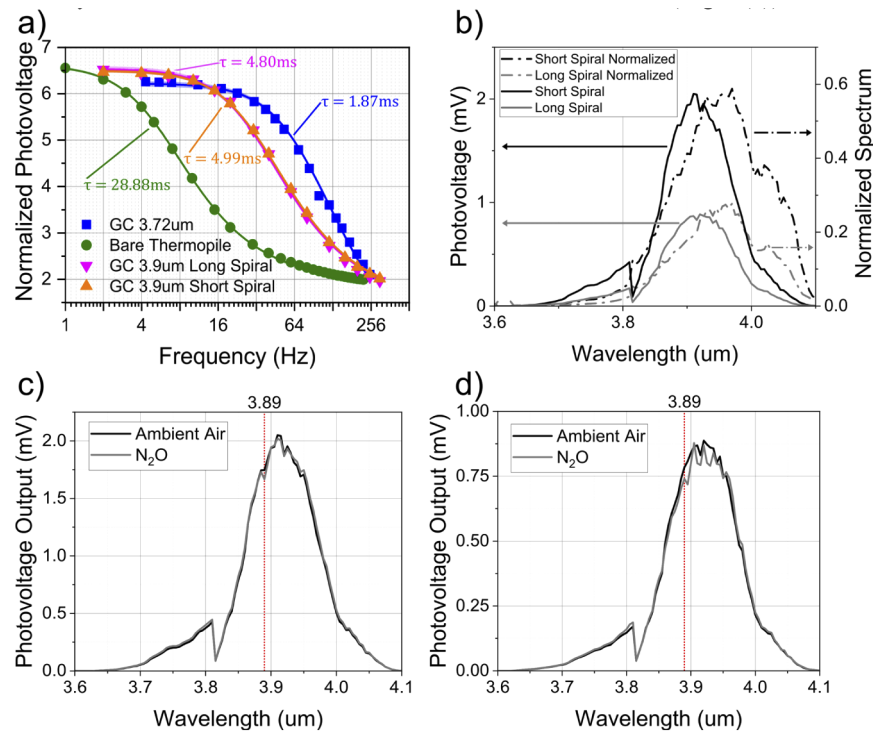


Fig. 8. (a) Frequency spectra of bare and bonded thermopiles. Solid lines are fitted low-pass filters. (b) Optical spectra of short and long spiral waveguides with grating couplers as measured (solid lines) and normalized to laser spectrum (dash-dotted lines). (c, d) Optical spectra of short (c) and long (d) spiral waveguides in ambient air conditions (black line) and in N₂O environment (grey line). 3.89 μm wavelength is labelled with red-dotted line in (c) and (d).

([41], Fig. 7) decreases with the presence of N₂O due to the evanescent field coupling between the waveguide and N₂O gas molecules surrounding the waveguide. The transmitted intensity at 3.89 μm can be used to detect the N₂O gas surrounding the waveguide. Figure 9 shows the time response from the thermopile output that is proportional to transmitted light throughout the waveguide. For both waveguides, the photovoltage output from thermopile decreases with the injection of N₂O (target) gas because of the decreased transmitted light intensity due to molecular absorption of N₂O. The signal recovers back to its original value once the PDMS chamber is flushed with CO₂ (reference) gas. The measurements were performed at different frequencies to observe the frequency dependence of signal to noise ratio (SNR). The noise decreases as the frequency increases, suggesting the presence of 1/f noise in the system. However, since the thermopile responsivity is also frequency dependent as shown in Fig. 8, the signal will also drop along with the noise as the chopper frequency is increased.

The study of the noise measured in the gas sensing measurement is necessary in order to understand the cause of the noise and to optimize the SNR for an increased performance. Intrinsic noise coming from the thermopile can be calculated with the Johnson noise provided in Eq. (4), whereas k_B is the Boltzmann constant, T is the operation temperature, R is the resistance and Δf is the measurement bandwidth. With thermopile resistance of 77 kOhm, operation temperature of 300 K (about room temperature) and measurement bandwidth of 10 Hz (using lock-in amplifier), the Johnson noise is equal to $v_n = 49.7 \text{ nV} \approx 0.05 \mu\text{V}$. We have measured signal (which is calculated from the photovoltage difference with and without N₂O presence) and noise with

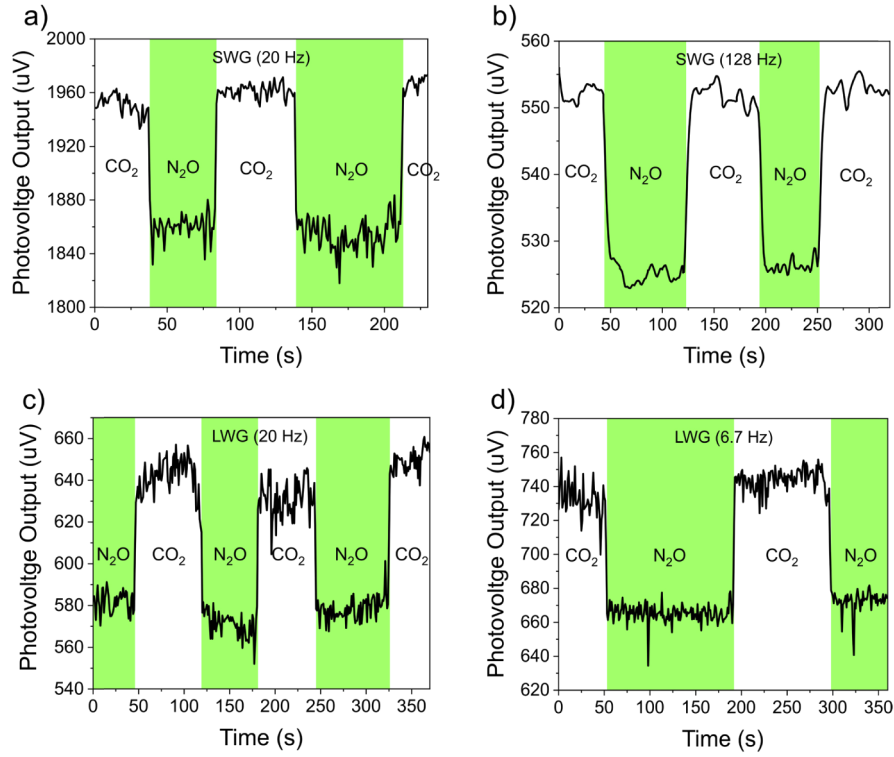


Fig. 9. Photovoltage response from thermopile with alternating injection of N_2O and CO_2 gasses into the PDMS micro-chamber. Short (a and b) and long (c and d) spiral waveguide responses to N_2O injection with different chopping frequencies.

respect to the frequency for a spiral waveguide design and calculated the SNR ratio (Fig. 10). We observed that the $1/f$ noise is the dominant noise in the low frequency range ($f < 15$ Hz) and the Johnson noise (frequency independent) is the dominant noise in the higher frequency range ($f > 15$ Hz). We attribute the $1/f$ noise coming from the measurement equipment (i.e. lock-in amplifier) and from the environmental coupling. The difference signal between with and without the presence of N_2O is calculated using the results in Fig. 9 and using Eq. (5) and 6 whereas V_1 is the photovoltage output with N_2O presence and V_2 is the photovoltage output without N_2O . ϵ is molar absorption in units of [L/mol/cm], η is evanescent field factor without any unit, c is the concentration in [mol/L], α is the propagation loss in [cm^{-1}], l is the interaction length of waveguide with gas molecules surrounding it which is equal to the length of the waveguide that is inside the PDMS gas chamber and l_0 is the remaining length of the waveguide without any gas interaction. With $c_1=c$ and $c_2=0$, normalized signal difference is calculated in Eq. (7). Note that normalized sensing signal is independent of frequency. Thus, the only frequency dependency comes from the responsivity which can be obtained from the measurement results (Fig. 8(a)).

$$v_n = \sqrt{4k_B TR \Delta f} \quad (4)$$

$$V_1 = \frac{P_0}{2} e^{-(\epsilon \eta c_1 l + \alpha(l+l_0))} R_v(f) \quad (5)$$

$$V_2 = \frac{P_0}{2} e^{-(\epsilon \eta c_2 l + \alpha(l+l_0))} R_v(f) \quad (6)$$

$$\frac{V_2 - V_1}{V_2} = 1 - e^{-\epsilon \eta c l} \quad (7)$$

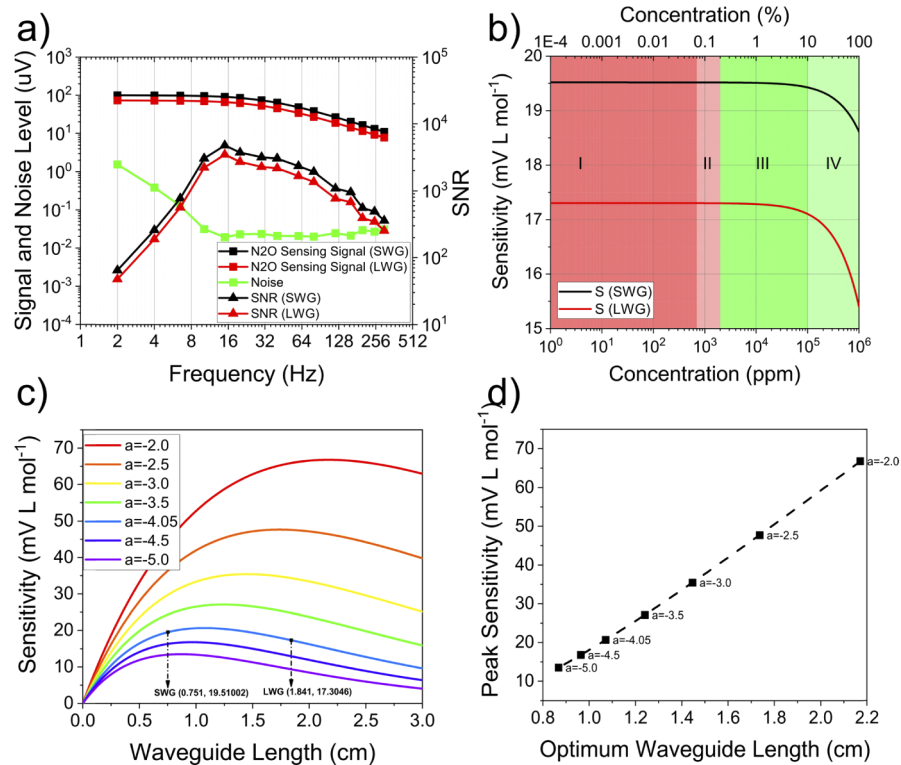


Fig. 10. a) Sensing signal and noise vs frequency for short (SWG) and long (LWG) spiral waveguides and SNR value. b) Sensitivity vs concentration for short and long spiral waveguides. c) Sensitivity vs waveguide length for different propagation losses (α in dB/cm). Short and long waveguide fabricated are marked. d) Relation between peak sensitivity and optimum waveguide length. As the propagation loss (α) decreases, the optimum waveguide length increases along with the peak sensitivity.

Hence, with noise and sensing signal measured from our system with respect to frequency, the signal to noise ratio (SNR) can also be plotted on the same graph. The SNR shows its maximum value at around 15 Hz where the signal is still close to its highest value and $1/f$ noise becomes negligible when compared to Johnson noise. At lower frequencies, the noise is high whereas signal is constant and at higher frequencies although the noise is low, the signal decreases with increased frequency and hence SNR achieves its highest value of 4700 and 3500 for short and long waveguides respectively. The normalized sensing signal (as provided in Eq. (7)) is measured to be 0.051, 0.049, 0.096 and 0.106 for sensing measurements presented in Figs. 9(a)–9(d) respectively. Hence, on the average we have 0.05 (5%) and 0.10 (10%) of signal change for short and long waveguides respectively. The long waveguide shows a better normalized responsivity due to a longer interaction with the air molecules. However, since short waveguide has higher signal output due to a lower total propagation loss, the sensing signal measured from short waveguide is still higher than that of the long waveguide (Fig. 10). Since both waveguides share the same thermopile, both measurements are subjected to the same noise level. Thus, the short waveguide shows a better SNR performance. When we compare the noise and SNR extracted in Fig. 10 with the noise and the SNR of gas sensing data presented in Fig. 9, we observe that the signal fluctuations in gas testing measurements are much higher than that of the measured noise presented in Fig. 10. The measured SNR values are 14.04, 20.83, 8.96 and 13.69 for data presented in Figs. 9(a)–9(d) respectively, whereas the extracted SNR values for

same measurements (according to measurement presented in Fig. 10) are 3700, 1000, 2700 and 560 respectively. We attribute signal fluctuations observed during gas sensing measurements to the concentration fluctuations of gasses flowing through the PDMS gas chamber causing unstable light intensity arriving at the thermopile device, resulting in a poor SNR value. However, in the actual setup where the sensor is operated in a diffusion mode rather than flow-through mode, such concentration fluctuations should be absent. Hence, high SNR values of 4700 and 3500 are expected for short and long waveguide devices when signal is chopped at 15 Hz.

The resolution of the gas sensor depends on the sensitivity of the overall system and noise. As discussed before, the noise can be reduced by chopping the illumination and using a lock-in technique to measure the output signal with a small bandwidth. On the other hand, the sensitivity depends on the responsivity of detector device (i.e. Responsivity, R_v) and sensitivity of the sensing element (i.e. waveguide). Hence, the overall sensitivity (S) can be defined as the change of the signal output (i.e. photovoltage) with respect to concentration change of the target molecule and can be calculated using Eq. (8). $\epsilon\eta c$ and $\epsilon\eta$ products can be extracted from gas sensing measurements (Fig. 9), using Eq. (7) and taking c (concentration) to be 0.0446 mol/L which assumes that the pressure inside PDMS gas chamber is 1 atm and the volume concentration of N_2O is 100%. Hence $\epsilon\eta c$ and $\epsilon\eta$ products are found to be 0.0632 cm^{-1} and $1.4169 \text{ Lmol}^{-1}\text{cm}^{-1}$ respectively. With our current fabrication, we observe a propagation loss of -3 to -5 dB/cm and a grating coupler efficiency of -10 dB [28]. With the measured data for short and long waveguide, we obtain a fitted propagation loss of $\sim 4.05 \text{ dB/cm}$ for the devices used. Measured parameters for fabricated devices were summarized in Table 1.

Table 1. Measured Parameters for Fabricated Devices

Parameter Type	Sensing		Optical		Electrical
Parameter [unit]	c [mol/L]	$\epsilon\eta$ [L/(mol cm)]	α [dB/cm]	Coupling Loss [dB]	3σ (LOD signal) [nV]
Value	0.0446	1.4169	-4.05	-10	150

Using the measured propagation loss (α) of -4.05 dB/cm , $\epsilon\eta$ product of $1.4169 \text{ Lmol}^{-1}\text{cm}^{-1}$, concentration (c) of 0.0446 mol/L, idle waveguide (non-sensing) length (l_0) of 0.992 cm and spiral waveguide (sensing) length (l) of 0.751/1.841 cm for short/long spiral waveguide, we calculate the limit of detection (LOD) of 1800ppm (0.18%) and 2000ppm (0.2%) for fabricated short and long waveguides. The LOD is defined as the signal difference ($V_2 - V_1$) between 0 ppm and LOD value whereas the difference is larger than $3\sigma = 0.15 \mu\text{V}$ (0.156 and 0.154 μV for the short and long waveguide respectively) with a lock-in bandwidth of 10 Hz. Resolution, as defined as difference between two measurement points that have 3σ of signal difference, is a function of the concentration since the sensitivity (as in Eq. (8)) depends on the concentration. However, the noise (σ) and hence resolution (3σ) does not. Sensitivity vs concentration curves for short and long spiral waveguides are shown on the same graph in Fig. 10(b). Area I, depicted in red, represents the region where the sensitivities of the sensors are high, but the signal level is below the Johnson noise level (i.e. $0.05 \mu\text{V}$). Area II, depicted in light red, represents the region where the signal is higher than noise level (σ) but lower than LOD (3σ). Area III, depicted in green, represents the region where sensitivities of the sensors are high, and the signal level is beyond LOD (3σ). Area IV, depicted in light green, is where the signal is higher than LOD but the sensitivities, and hence the resolutions, start to decrease, achieving lowest the resolution of 1900ppm and 2200 ppm (for short and long WG) near 100% concentration.

$$S = \frac{-dV}{dc} = \frac{P_0}{2} \epsilon\eta c l e^{-\epsilon\eta c l - \alpha(l+l_0)} R_v(f) \quad (8)$$

The length of the waveguide is an important parameter for having an optimum sensor design. Although the purpose of this approach is to have an integrated system rather than waveguide

optimization, we have calculated the optimum length for the maximum sensitivity, keeping the idle waveguide length the same (l_0 , waveguide part which stays outside of the PDMS gas chamber). Figure 10(c) shows the calculated results of the sensor detection sensitivities of the sensor near the 2000ppm region for different propagation loss values (α in dB/cm). As calculated previously, our propagation loss is -4.05 dB/cm which is indicated by the blue curve and the short and long spiral waveguide designs are also marked on the curve. Although the long spiral waveguide, with a sensitivity of $S = 17.30$ mVLmol $^{-1}$ at $\{l = 1.841$ cm, $l_0 = 0.992$ cm $\}$, is slightly off from the optimum value of $S = 20.64$ mVLmol $^{-1}$, which occurs at $\{l = 1.072$ cm, $l_0 = 0.992$ cm $\}$, the short spiral waveguide is closer to the optimum value with sensitivity of $S = 19.51$ mVLmol $^{-1}$ at $\{l = 0.751$ cm, $l_0 = 0.992$ cm $\}$. As can be observed from the graph, the propagation loss is a dominant factor in having a high sensitivity. Figure 10(d) shows the extracted peak sensitivities for different propagation losses and the optimum waveguide length. As propagation loss decreases, the optimum waveguide length and hence responsivity increases. Decreasing the propagation loss from -4 dB/cm to -2 dB/cm [12,42,43] will provide a three-fold enhancement in sensitivity. Also disposing any (dummy) waveguide parts that do not interact with air (i.e. $l_0=0$) increases the sensitivity of both SWG and LWG by 2.5 times due to the elimination of excess propagation losses. The propagation loss can further be reduced by reducing the scattering loss via having a smoother waveguide surface after the RIE [44]. However, in the MIR, the absorption loss due to SiO $_2$ layer below the waveguide is the dominating factor for propagation loss [45,46]. Thus, the best way would be to suspend the waveguide via either vapored hydrofluoric acid etching (VHF) or via wet HF etching (buffered oxide etch (BOE) or diluted HF (DHF)) [47,48]. This would not only eliminate oxide absorption, but it also would also increase the evanescent field factor (η) by increasing the evanescent field volume that interacts with air molecules surrounding waveguide. Table 2 provides a comparison for fabricated short and long waveguide devices.

Table 2. Summary Table for Short and Long Waveguides

Parameter [unit]	l_0 [cm]	l [cm]	SNR (15 Hz) [-]	S [mVL/mol]	LOD [ppm]
SWG	0.992	0.751	4700	19.51	1800
LWG	0.992	1.841	3500	17.30	2000

5. Conclusion

We reported the integration of a broadband thermopile IR detector with a mid-IR waveguide using flip-chip bonding technology. The integration is realized by Al-wedge forming on the Au-pads and thermo-compression bonding of the Al-interface. This integration allows a spacer gap of 10 μ m between the two integrated chips and provides an electrical connection to thermopile. For our first device designed at 3.72 μ m, we have measured a peak DC responsivity of 69 mV/W with an 11 mm waveguide. We have demonstrated N $_2$ O gas detection via a second device with a grating coupler designed at 3.90 μ m. Fabricated waveguides support SNR values of 4700 and 3500 at 15 Hz chopping frequency which correspond to 1800 and 2000ppm resolutions (for SWG and LWG respectively) with a 3σ (99.7%) confidence. MEMS-based broadband IR detector integration with waveguides along with an IR source integration will pave the way for fully integrated miniaturized in-plane spectrometers.

Funding

National Research Foundation (NRF2015-NRF-ISF001-2620, NRF-CRP15-2015-02).

Acknowledgments

The authors would like to thank Prof. Aaron Thean and Dr. Yida Li for the access and training of die bonder used for the flip-chip bonding process.

Disclosures

The authors declare no conflicts of interest.

References

1. J. D. Fenske and S. E. Paulson, "Human Breath Emissions of VOCs," *J. Air Waste Manage. Assoc.* **49**(5), 594–598 (1999).
2. S. C. Lee, M. Y. Chiu, K. F. Ho, S. C. Zou, and X. Wang, "Volatile organic compounds (VOCs) in urban atmosphere of Hong Kong," *Chemosphere* **48**(3), 375–382 (2002).
3. D. Hasan and C. Lee, "Hybrid Metamaterial Absorber Platform for Sensing of CO₂ Gas at Mid-IR," *Adv. Sci.* **5**(5), 1700581 (2018).
4. Z. Ren, Y. Chang, Y. Ma, K. Shih, B. Dong, and C. Lee, "Leveraging of MEMS Technologies for Optical Metamaterials Applications," *Adv. Opt. Mater.* **8**(3), 1900653 (2020).
5. T. Zhang, M. B. Nix, B.-Y. Yoo, M. A. Deshusses, and N. V. Myung, "Electrochemically Functionalized Single-Walled Carbon Nanotube Gas Sensor," *Electroanalysis* **18**(12), 1153–1158 (2006).
6. J. Fergus, "Materials for high temperature electrochemical NO_x gas sensors," *Sens. Actuators, B* **121**(2), 652–663 (2007).
7. C. Wang, L. Yin, L. Zhang, D. Xiang, and R. Gao, "Metal Oxide Gas Sensors: Sensitivity and Influencing Factors," *Sensors* **10**(3), 2088–2106 (2010).
8. G. Jiang, M. Golezdzinowski, F. J. E. Comeau, H. Zarrin, G. Lui, J. Lenos, A. Veileux, G. Liu, J. Zhang, S. Hemmati, J. Qiao, and Z. Chen, "Free-Standing Functionalized Graphene Oxide Solid Electrolytes in Electrochemical Gas Sensors," *Adv. Funct. Mater.* **26**(11), 1729–1736 (2016).
9. J. Hodgkinson, R. Smith, W. O. Ho, J. R. Saffell, and R. P. Tatam, "Non-dispersive infra-red (NDIR) measurement of carbon dioxide at 4.2 μm in a compact and optically efficient sensor," *Sens. Actuators, B* **186**, 580–588 (2013).
10. Kum-Pyo Yoo, Kwang-Ho Kwon, Nam-Ki Min, Si-Dong Kim, and Woo-Seok Choi, "A front-side dry-etched thermopile detector with 3–5 μm infrared absorber and its application to novel NDIR CO₂ gas sensors," in 2008 IEEE SENSORS (2008), pp. 894–897.
11. W.-C. Lai, S. Chakravarty, X. Wang, C. Lin, and R. T. Chen, "On-chip methane sensing by near-IR absorption signatures in a photonic crystal slot waveguide," *Opt. Lett.* **36**(6), 984–986 (2011).
12. L. Tombez, E. J. Zhang, J. S. Orcutt, S. Kamlapurkar, and W. M. J. Green, "Methane absorption spectroscopy on a silicon photonic chip," *Optica* **4**(11), 1322–1325 (2017).
13. P. Su, Z. Han, D. Kita, P. Becla, H. Lin, S. Deckoff-Jones, K. Richardson, L. C. Kimerling, J. Hu, and A. Agarwal, "Monolithic on-chip mid-IR methane gas sensor with waveguide-integrated detector," *Appl. Phys. Lett.* **114**(5), 051103 (2019).
14. Y. Ma, B. Dong, B. Li, J. Wei, Y. Chang, C. P. Ho, and C. Lee, "Mid-Infrared Slow Light Engineering and Tuning in 1-D Grating Waveguide," *IEEE J. Sel. Top. Quantum Electron.* **24**(6), 1–8 (2018).
15. B. Dong, T. Hu, X. Luo, Y. Chang, X. Guo, H. Wang, D.-L. Kwong, G.-Q. Lo, and C. Lee, "Wavelength-Flattened Directional Coupler Based Mid-Infrared Chemical Sensor Using Bragg Wavelength in Subwavelength Grating Structure," *Nanomaterials* **8**(11), 893 (2018).
16. Y. Ma, B. Dong, B. Li, K.-W. Ang, and C. Lee, "Dispersion engineering and thermo-optic tuning in mid-infrared photonic crystal slow light waveguides on silicon-on-insulator," *Opt. Lett.* **43**(22), 5504–5507 (2018).
17. S. Simhony, E. M. Kosower, and A. Katzir, "Novel attenuated total internal reflectance spectroscopic cell using infrared fibers for aqueous solutions," *Appl. Phys. Lett.* **49**(5), 253–254 (1986).
18. H. Paul and G. Kychakoff, "A fiber-optic evanescent field absorption sensor," in *International Congress on Applications of Lasers & Electro-Optics* (Laser Institute of America, 1986), pp. 27–32.
19. P. H. Paul and G. Kychakoff, "Fiber-optic evanescent field absorption sensor," *Appl. Phys. Lett.* **51**(1), 12–14 (1987).
20. P. Ma, D.-Y. Choi, Y. Yu, X. Gai, Z. Yang, S. Debbarma, S. Madden, and B. Luther-Davies, "Low-loss chalcogenide waveguides for chemical sensing in the mid-infrared," *Opt. Express* **21**(24), 29927–29937 (2013).
21. P. T. Lin, H. Jung, L. C. Kimerling, A. Agarwal, and H. X. Tang, "Low-loss aluminium nitride thin film for mid-infrared microphotonic: Low-loss aluminium nitride thin film for mid-infrared microphotonic," *Laser Photonics Rev.* **8**(2), L23–L28 (2014).
22. P. Ma, D.-Y. Choi, Y. Yu, Z. Yang, K. Vu, T. Nguyen, A. Mitchell, B. Luther-Davies, and S. Madden, "High Q factor chalcogenide ring resonators for cavity-enhanced MIR spectroscopic sensing," *Opt. Express* **23**(15), 19969–19979 (2015).
23. A. Spott, J. Peters, M. L. Davenport, E. J. Stanton, C. D. Merritt, W. W. Bewley, I. Vurgaftman, C. S. Kim, J. R. Meyer, J. Kirch, L. J. Mawst, D. Botez, and J. E. Bowers, "Quantum cascade laser on silicon," *Optica* **3**(5), 545–551 (2016).

24. G. K. Veerabathran, S. Sprengel, A. Andrejew, and M.-C. Amann, "Room-temperature vertical-cavity surface-emitting lasers at 4 μm with GaSb-based type-II quantum wells," *Appl. Phys. Lett.* **110**(7), 071104 (2017).
25. C. Consani, C. Ranacher, A. Tortschanoff, T. Grille, P. Irsigler, and B. Jakoby, "Mid-infrared photonic gas sensing using a silicon waveguide and an integrated emitter," *Sens. Actuators, B* **274**, 60–65 (2018).
26. J. Wang, J. Hu, P. Becla, A. M. Agarwal, and L. C. Kimerling, "Resonant-cavity-enhanced mid-infrared photodetector on a silicon platform," *Opt. Express* **18**(12), 12890–12896 (2010).
27. R. Fain, S. A. Miller, M. Yu, A. G. Griffith, J. Cardenas, and M. Lipson, "CMOS-compatible mid-infrared silicon detector," in *2017 Conference on Lasers and Electro-Optics (CLEO) (2017)*, pp. 1–2.
28. N. Youngblood, C. Chen, S. J. Koester, and M. Li, "Waveguide-integrated black phosphorus photodetector with high responsivity and low dark current," *Nat. Photonics* **9**(4), 247–252 (2015).
29. L. Huang, B. Dong, X. Guo, Y. Chang, N. Chen, X. Huang, W. Liao, C. Zhu, H. Wang, C. Lee, and K.-W. Ang, "Waveguide-Integrated Black Phosphorus Photodetector for Mid-Infrared Applications," *ACS Nano* **13**(1), 913–921 (2019).
30. H. Lin, Z. Luo, T. Gu, L. C. Kimerling, K. Wada, A. Agarwal, and J. Hu, "Mid-infrared integrated photonics on silicon: a perspective," *Nanophotonics* **7**(2), 393–420 (2017).
31. F. Tankut, M. H. Cologlu, H. Ozturk, G. Cilbir, O. S. Akar, and T. Akin, "A 160 \times 120 LWIR-band CMOS Infrared (CIR) microbolometer," in *Infrared Technology and Applications XLV* (International Society for Optics and Photonics, 2019), Vol. 11002, p. 110021Q.
32. X. Cai, A. B. Sushkov, R. J. Suess, M. M. Jadidi, G. S. Jenkins, L. O. Nyakiti, R. L. Myers-Ward, S. Li, J. Yan, D. K. Gaskill, T. E. Murphy, H. D. Drew, and M. S. Fuhrer, "Sensitive room-temperature terahertz detection via the photothermoelectric effect in graphene," *Nat. Nanotechnol.* **9**(10), 814–819 (2014).
33. G. Skoblin, J. Sun, and A. Yurgens, "Graphene bolometer with thermoelectric readout and capacitive coupling to an antenna," *Appl. Phys. Lett.* **112**(6), 063501 (2018).
34. H. Zhou, P. Kropelnicki, and C. Lee, "Characterization of nanometer-thick polycrystalline silicon with phonon-boundary scattering enhanced thermoelectric properties and its application in infrared sensors," *Nanoscale* **7**(2), 532–541 (2015).
35. H. Zhou, P. Kropelnicki, and C. Lee, "CMOS Compatible Midinfrared Wavelength-Selective Thermopile for High Temperature Applications," *J. Microelectromech. Syst.* **24**(1), 144–154 (2015).
36. J. H. Lau, "Recent Advances and New Trends in Flip Chip Technology," *J. Electron. Packag.* **138**(3), 030802 (2016).
37. M. S. Yazici, D. Hasan, B. Dong, F. Sun, and C. Lee, "Integration of Thermopile on a Mid IR Waveguide," in *2019 International Conference on Optical MEMS and Nanophotonics (OMN) (2019)*, pp. 108–109.
38. A. R. Ravishankara, J. S. Daniel, and R. W. Portmann, "Nitrous Oxide (N₂O): The Dominant Ozone-Depleting Substance Emitted in the 21st Century," *Science* **326**(5949), 123–125 (2009).
39. M. J. Kampschreur, H. Temmink, R. Kleerebezem, M. S. M. Jetten, and M. C. M. van Loosdrecht, "Nitrous oxide emission during wastewater treatment," *Water Res.* **43**(17), 4093–4103 (2009).
40. M. Rosen, "Nitrous oxide for relief of labor pain: A systematic review," *Am. J. Obstet. Gynecol.* **186**(5), S110–S126 (2002).
41. N. O. of D. and Informatics, "NIST Chemistry WebBook," <https://webbook.nist.gov/chemistry/>.
42. F. Sun, J. Wei, B. Dong, Y. Ma, Y. Chang, H. Tian, and C. Lee, "Coexistence of air and dielectric modes in single nanocavity," *Opt. Express* **27**(10), 14085–14098 (2019).
43. A. Gutierrez-Arroyo, E. Baudet, L. Bodiou, J. Lemaitre, I. Hardy, F. Fajjan, B. Bureau, V. Nazabal, and J. Charrier, "Optical characterization at 7.7 μm of an integrated platform based on chalcogenide waveguides for sensing applications in the mid-infrared," *Opt. Express* **24**(20), 23109–23117 (2016).
44. N. Carlie, J. D. Musgraves, B. Zdyrko, I. Luzinov, J. Hu, V. Singh, A. Agarwal, L. C. Kimerling, A. Canciamilla, F. Morichetti, A. Melloni, and K. Richardson, "Integrated chalcogenide waveguide resonators for mid-IR sensing: leveraging material properties to meet fabrication challenges," *Opt. Express* **18**(25), 26728–26743 (2010).
45. T. Hu, B. Dong, X. Luo, T.-Y. Liow, J. Song, C. Lee, and G.-Q. Lo, "Silicon photonic platforms for mid-infrared applications [Invited]," *Photonics Res.* **5**(5), 417–430 (2017).
46. B. Dong, X. Luo, S. Zhu, T. Hu, M. Li, D. Hasan, L. Zhang, S. J. Chua, J. Wei, Y. Chang, Y. Ma, P. Vachon, G.-Q. Lo, K. W. Ang, D.-L. Kwong, and C. Lee, "Thermal annealing study of the mid-infrared aluminum nitride on insulator (AlNOI) photonics platform," *Opt. Express* **27**(14), 19815–19826 (2019).
47. Z. Cheng, X. Chen, C. Y. Wong, K. Xu, C. K. Y. Fung, Y. M. Chen, and H. K. Tsang, "Focusing subwavelength grating coupler for mid-infrared suspended membrane waveguide," *Opt. Lett.* **37**(7), 1217–1219 (2012).
48. J. Kang, Z. Cheng, W. Zhou, T.-H. Xiao, K.-L. Gopalakrishna, M. Takenaka, H. K. Tsang, and K. Goda, "Focusing subwavelength grating coupler for mid-infrared suspended membrane germanium waveguides," *Opt. Lett.* **42**(11), 2094–2097 (2017).